Powder Technology 341 (2019) 126–139

Contents lists available at ScienceDirect

Powder Technology

journal homepage: www.elsevier.com/locate/powtec

Wet granular flow control through liquid induced cohesion

Ahmed Jarray [a,b,*], Vanessa Magnanimo [a], Stefan Luding [a]

[a] Multi Scale Mechanics (MSM), University of Twente, NL-7500 AE, Enschede, The Netherlands
[b] Research Center Pharmaceutical Engineering GmbH, Graz, Austria

ARTICLE INFO

Article history:
Received 7 October 2017
Received in revised form 26 January 2018
Accepted 19 February 2018
Available online 24 February 2018

Keywords:
Wet granular flow
Capillary forces
Rotating drum
Scaling
Granulation

ABSTRACT

Liquid induced cohesion has a significant effect on the flow characteristics of wet granular assemblies. The strength of capillary forces between the particles can be continuously tuned by making the glass beads hydrophobic via chemical silanization. Main results of rotating drum experiments are that stronger liquid-induced cohesion decreases the width of the flowing region, the velocity of the particles at the free surface and the local granular temperature, but in contrast, increases the width of the creeping region as well as the dynamic angle of repose. Our proposed scaling methodology yields invariant bed flow characteristics for different particle sizes in the flow regimes considered (rolling and cascading regimes), and thus allows to control the flow.

1. Introduction

Wet granular flows are ubiquitous in nature (e.g. mud flow, debris flow and avalanches) with direct application to numerous industrial processes (e.g. coating, granulation and fertilizer production). A simple and practical geometry to study the flow of granular materials is the rotating drum. This apparatus has been extensively studied by many researchers including Henein et al. [1] who established a relationship between the flow of particles in a drum and the Froude number and categorized it into six flow modes; slipping, slumping, rolling, cascading, cataracting, and centrifuging. At low rotation speed of the drum, Rajchenbach [2] correlated the dynamic angle of repose to the rotation speed. Taberlet et al. [3] derived an equation to describe the S shape of the granular pile in a drum. Orpe et al. [4] found that the flowing layer is symmetric at low Froude number (Fr) and large ratios of particle size to drum radius ($2r/D$). Further on, Elperin and Vikhansky [5] proposed a model for describing the bed flow using a Mohr-Coulomb failure criterion. Sheng et al. [6] investigated the effect of particles surface roughness on the bed flow. At low rotation speed, below 10 rpm in their device geometry ($Fr = 0.17$), the surface of the pile in their rotating drum was flat with a flow speed that decreases from the bed surface downwards. Nakagawa et al. [7] measured the velocity of the flow in a rotating drum by resonance imaging. For large rotation rate, they showed that the surface is S-shaped and the flow rate is usually the highest in the middle of the flowing layer where the angle of the slope is the steepest. An almost stationary bulk region usually referred to as the creeping region can also be found below the flowing region. Komatsu et al. [8] measured the creeping region and found that the velocity rapidly decreases with depth in this region. Jain et al. [9] found that the velocity gradients and thicknesses of the flowing layer do not vary when the width of the drum is between 2 and 30 times the size of the particles.

While, most of these studies focused on the flow of dry particles, mechanisms governing particle flow in wet systems remain poorly understood. In fact, when a small amount of liquid is added to a pile of particles, pendular bridges form and the particles are attracted by capillary forces, creating complex structures and flow behavior. The work of Tegzes et al. [10] and Schubert [11] for instance showed that the capillary force strongly influences and changes the flow motion of particles. Brewster et al. [12] found that the presence of interparticle cohesion reduces the concavity of the free flowing, pushing it towards a flat or even slightly convex shape. Through experiments in a shear cell device, Chou et al. [13] found that the liquid content increases the segregation of particles in a rotating drum. Using Discrete Element Method (DEM) simulation, Liu et al. [14] investigated the effect of surface tension on the flow of wet particles. They showed that the maximum angle of stability of the flow in a rotating drum increases with the surface tension. Samadani and Kudrolli [15] showed that the flow in wet granular systems is controlled by the number of liquid bridges. Roy et al. [16] studied the effect of liquid bridge volume and surface tension of the liquid on the macroscopic properties of the bulk materials, and established a micro-macro correlation. Using a split bottom shear cell, Mani et al. [17] showed that liquid concentration decreases inside a shear band. In a more recent work, Jarray et al. [18] investigated the effect of interstitial liquid on the dynamic angle of repose and showed that it is possible to scale the flow and obtain similar dynamic angles of repose for different particle

* Corresponding author at: Multi Scale Mechanics (MSM), University of Twente, NL-7500 AE Enschede, The Netherlands.
E-mail address: a.jarray@utwente.nl (A. Jarray).

https://doi.org/10.1016/j.powtec.2018.02.045

sizes by modifying the surface properties of the particles. Despite these efforts, the effect of the complex network of capillary bridges on the macroscopic properties of granular assemblies under dynamic conditions remains obscure and, therefore, must be better understood to be able to control wet granular flows.

The aim of this work is to explore the effect of liquid induced cohesion on the flow properties of wet granular assemblies at different particle sizes in order to establish a scaling methodology of the flow of wet particles in a rotating drum. We complement our previous work [18] and focus mainly on macroscopic phenomena associated with the collective behaviour of particles. In their investigation of the flow of wet granular assemblies in a rotating drum, several authors including Nowak et al. [19], Xu et al. [20], Soria-Hoy et al. [21] and Tagzes et al. [10] varied the liquid content. In this work, however, rather than changing the liquid content, we vary experimentally the capillary force and we use the variability of the contact angle to vary the strength of capillary cohesion. Chemical silanization is used to alter the surface properties of the glass beads allowing to obtain a wide range of capillary forces between the particles when mixed with a small amount of ethanol-water mixtures. We begin by investigating and classifying the influence of the particle size, rotation speed and the capillary forces on the bed flow in dry and diverse wet systems, and we show how liquid induced cohesion affects the free flowing layer and the dynamic angle of repose. Then, we explore the effect of the capillary force on the creeping zone and the free surface flow by measuring the granular flow fields using Particle Image Velocimetry (PIV). Flow characteristics, such as velocity and granular temperature are explored in detail. Finally, in Section 3.3, we propose a scaling approach that ensures particle flow similarity for different particle sizes.

2. Materials and methods

2.1. Capillary force and silanization procedure

The structure of wet granular assemblies is determined by a complex network of mechanical contacts and non-uniform liquid bridges connecting adjacent particles. Such bridges, for instance, keep a sandcastle standing [22] and determine the flow properties of wet granular materials. The dynamic behavior of wet granular materials can display a complex dependence on the amount and type of liquid present [23–25]. In this work, we will focus on the pendular state [26,27], where liquid bridges are small and do not merge. This results in a pairwise capillary force that displays little variations with the liquid volume towards small separation distances or at particle contact [28,29]. For two particles in contact (i.e. d~0, with d the distance between the two particles) with the same radius (see Fig. 1), the capillary force depends linearly on the product of contact angle cosθ, the surface tension γ and the radius r [30,31].

$$F_c = 2\pi\gamma r \cos\theta. \quad (1)$$

Fig. 1 shows the liquid bridge between two identical spheres. Here, θ is the liquid contact angle at the solid–liquid interfaces. Relatively small liquid bridges are considered and gravitational deformations of the menisci are neglected.

In order to characterize the capillary forces generated by liquid bridges and their effect on the flow of granular assemblies, we consider separately the roles of particle size, contact angle, and surface tension. Similarly to the work of Raux et al. [32], we treat the surface of the glass beads via silanization to increase their hydrophobicity (i.e. we increase the contact angle θ). Using mixtures of ethanol-water as interstitial liquid and glass beads with different hydrophobicity, the capillary force between two adjacent beads can be tuned over a wide range.

Silanization is based on the adsorption, self-assembly and covalent binding of silane molecules onto the surface of glass beads. Chemical compounds used for silanization are: silanization solution I~5% (*V*/*V*) (5% in volume of Dimethyldichlorosilane in Heptane, Selectophore), Hydrochloric acid (HCl, 0.1 mol), Acetone and Ethanol.

The procedure for increasing the beads hydrophobicity is as follows: First, glass beads, initially hydrophilic, are cleaned for at least one hour by immersion into freshly prepared HCl solution under agitation using a rotor-stator homogenizer. Then, they are rinsed thoroughly with deionized water and oven dried for 3 h at 60 °C. Afterwards, the freshly cleaned glass beads are immersed in the silanisation solution under low agitation at room temperature for one hour. The inorganic functionality of the silane reacts with the different OH groups obtained after cleaning with HCl and forms Si—OH groups that make the glass beads hydrophobic. Finally, the glass beads are rinsed with acetone and allowed to air-dry under a fume hood for 24 h.

To measure the contact angle, θ, liquid droplets are placed on a glass surface. Then, pictures of the droplet are taken using a MotionBLITZ EoSens camera with close-up lenses. The contact angle is then deduced by image analysis using LBADSA plugin in the open source imageJ software. The LBADSA plugin is based on the fitting of the Young-Laplace equation to the image data [33]. As shown in Fig. 2, water—ethanol mixtures with different ethanol fractions give various contact angles, which continuously decrease from 96° to 30° for silanized beads and from 53° to 6° for untreated glass as the ethanol fraction in the liquid increases: the higher the contact angle, the lower the wettability of the hydrophobic glass surface.

In Fig. 3, we plot the capillary force F_c defined in Eq. (1) against the volume fraction of ethanol in the water-ethanol mixture. Surface tension values are taken from Ref. [34]. Since the contact angle θ affects the strength of the capillary force, here, differently from e.g [35,36]., the variability of the contact angle is taken into account. The Bond number *Bo* (Eq. 2), represents the ratio of the capillary force to the gravitational force, is also shown along the vertical axis in Fig. 3 as a function the water-ethanol fraction.

$$Bo = \frac{3\gamma\cos\theta}{2r^2\rho_p g}, \quad (2)$$

where ρ_p is the density of the particle.

The capillary force decreases with increasing ethanol concentration for particles with unmodified glass surface, while F_c increases in the case of silanized glass beads, in agreement with the literature [37]. This allows controlling the strength of the capillary force between the glass beads in the rotating drum. Overall, one dry and six different wet experiments were performed in the rotating drum for different particle sizes (0.85, 1.25 and 2 mm in radius). The wet cases correspond to the 6 left points in Fig. 2. Details of the experiments are given in Table 1.

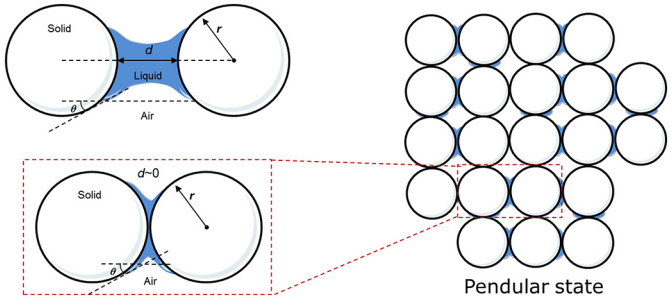

Fig. 1. Schematic of pendular liquid bridges between two identical spherical particles (Left) and the pendular state (right).

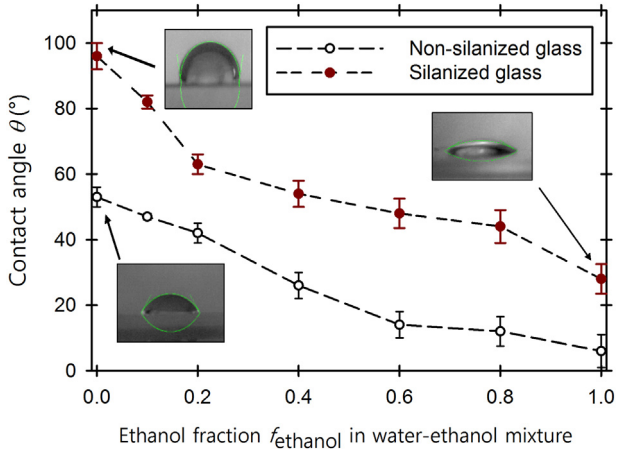

Fig. 2. Contact angles of water-ethanol mixtures as a function of the ethanol fraction on silanized and non-silanized glass.
Adapted from Ref. [18].

2.2. The drum apparatus

Samples of silanized and non-silanized glass particles, as described above in Table 1, are placed in a rotating drum (see Fig. 4). We use the new updated version of the drum setup that was used to study segregation by Windows-Yule et al. [38]. The drum is made by a cylinder of 121 mm inner diameter, 22 mm width, larger than $6.4 \times r$ of all the particles used, and held between two circular plexiglass (PMMA) plates of 5 mm thickness to allow optical access (frontal view in Fig. 4 (a)). The drum is placed on a horizontal rotating axis driven by a variable-speed motor, aligned with the z axis. The PMMA walls of the drum are coated with Fluorinated Ethylene Propylene (FEP) coating manufactured by CS Hyde Company to prevent wet glass beads from sticking on the wall. Images of the rotating drum are recorded using a MotionBLITZ EoSens high speed camera working at a speed of 460 fps. For a quasi-two-dimensional rotating drum, Jain et al. [39] argued that the width of the drum in the z direction should be larger than $6.4 \times r$, with r the average radius of the particles, to neglect the front and back wall friction on the flow characteristics, but also should be lower than $18.8 \times r$ in order to suppress axial effects [40]. Consequently, the velocity field can be assumed to be two dimensional. The angle between the top surface of the rolling bed and the horizontal plane is called the dynamic angle of repose θr (Fig. 4 (b)). We refer to the angle at the bottom of the drum as the lower dynamic angle of repose θs. The axis y is normal to the flow, and we refer to the zone in the middle of the bed along the y direction as the median region (See Fig. 4 (b)).

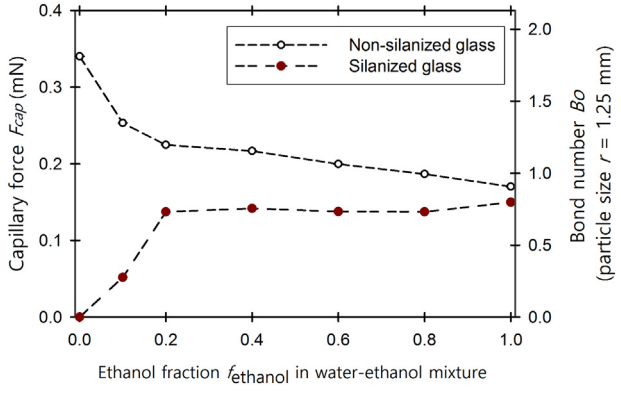

Fig. 3. Capillary forces Fc of water-ethanol mixtures as a function of the ethanol fraction on silanized and non-silanized glass beads. Fc is calculated using Eq. (1), and Bo obtained from Eq. (2).

After each experiment, the drum is dried in an oven for one hour to let the remaining liquid from the previous experiment evaporate. Experiments were restricted to the rolling and cascading regimes in the range $0.05 < Fr < 0.4$, where the Froude number;

$$F_r = \sqrt{\frac{\omega^2 D}{2g}}, \tag{3}$$

represents the ratio of centrifugal to gravitational acceleration [41]. In Eq. (3), ω is the angular speed of the drum, D its diameter andgthe acceleration due to gravity. Experiments are conducted using a selected set of monodisperse glass beads of density 2500 kg/m^3 with Young's modulus $Y = 6.4 \times 10^{10}$ N/m^2 and Poisson ratio $\nu = 0.2$. Parameters and characteristics of the drum and the glass beads are summarized in Table 2.

Throughout this work, a reference amount of liquid V_{liq} is mixed with the same mass of particles (i.e. 125 g of particles corresponding to a bed volume $V_{bed} = 0.00035$ m^3) in the rotating drum. Using $V_{liq} = 4$ ml as interstitial liquid for all the particle sizes used (i.e. 0.85, 125 and 2 mm), the bed saturation;

$$s = \frac{k\rho_p(1-\xi)}{\rho_l \xi} = \frac{V_{liq}}{V_{bed}\xi}, \tag{4}$$

where ξ is the porosity of the bed in the rotating drum, k represents the mass fraction of liquid, ρ_p and ρ_l are the density of the particle and the liquid respectively. In our case, the bed saturation is below 25%, suggesting that we are in the pendular state [42,43].

2.3. Image post-processing

The images, acquired using the high-speed camera, are post-processed using the particle tracking package Trackmate within the Fiji ImageJ distribution [44]. In Fig. 5, we show the images post-processing steps used in this work to compute the dynamic angle of repose and the velocity field. First, we removed the background from each image and adjusted the lighting in order for the moving particles to become markedly brighter than the background. Then, the Trackmate package is used to detect the position of the particles in every frame. Particles outlines (i.e. spots) that stand out from the background were segmented and identified based on the difference of Gaussians approach [45] with an estimated particle diameter of ~8 pixels. Detected particles are represented as spots or spheres with an initially constant radius (see Fig. 5). The detected spots are then imported in ParaView [46] and converted into a sequence of tables. Then, the dynamic angle of repose is numerically computed by linear regression of the positions of the particles using an in-house python code filter. The python code detects the particles which are on the surface of the flow using a concave-hull algorithm (the code is attached as supplementary material) [47].

Particle Image Velocimetry (PIV) in the PIVlab package [48] in Matlab is used to measure the particles displacements and vector fields. PIV is a non-intrusive, image-based measurement technique where a deformation field is detected by comparing two consecutive images. First, the drum which represents the Area of Interest (AOI) is cut out of the digital image and divided into small sub-areas called interrogation cells. Then, every two successive frames are combined into a single new frame. To obtain the velocity vectors between the interrogation areas in the first and second image, a multi-pass correlation algorithm with a final interrogation size of 8 pixels is used, which is of the order of the particle size. An interrogation size around the order of the particle size has also been adopted by previous authors [49,50] to ensure smooth and reliable results. For each

Table 1
Experimental cases used throughout this work. Wet cases correspond to the 6 left points in Fig. 2.

Cases	Wet or dry	Silanized	Ethanol fraction	Capillary forces F_c (mN, for particle size $r = 1.25$ mm)	Bond number Bo (for particle size $r = 1.25$ mm)
Case 1	Dry	No	–	–	–
Case 2	Wet	Yes	0	0	0
Case 3	Wet	Yes	0.1	0.0517	0.2755
Case 4	Wet	Yes	0.2	0.1372	0.7315
Case 5	Wet	No	0.2	0.2247	1.1974
Case 6	Wet	No	0.1	0.2533	1.3500
Case 7	Wet	No	0	0.3403	1.8134

experimental run, we applied PIV analysis for over 120 consecutive images (i.e. over the period of 0.33 s). The final time-averaged velocity vectors field is obtained by averaging all velocity fields that are calculated using each newly combined image (see Fig. 5). The data obtained from PIV are then imported in ParaView for further post-processing. Using several python scripts, the granular temperature and the flow speed are computed, smoothed using Point Volume Interpolation [51,52] and visualized in ParaView (see Section 2.4). For the smoothing, a Gaussian kernel is used, with a cut-off equal to 6 times the particle radius (i.e. 6r).

2.4. Properties computation

The data obtained from PIV are used to calculate the flow speed and the granular temperature. The flow speed is a measure of flowability and mobility of particles in an avalanche or during continuous flow, and is calculated, for a particle i, using the following formula:

$$\varphi_i = \sqrt{\left(v_{i,x} - v_{i,\omega x}\right)^2 + \left(v_{i,y} - v_{i,\omega y}\right)^2}, \tag{5}$$

where $\vec{v}_i = (v_{i,x},\ v_{i,y})$is the particle velocity and $\vec{v}_{i\omega} = (v_{i,\omega x},\ v_{i,\omega y})$is the angular velocity of particle i due to the rotation of the drum.

The granular temperature T of particles quantifies the inter-particle random motions caused by continuous collisions between particles or between particles and boundaries. Measurements of T are useful to elucidate the variable dynamic nature of granular material flows. Since the granular temperature is analogous to the thermodynamic temperature, it should be expected that T is the highest in the regions where the material exhibits fluid-like flow and lowest in those regions where the behaviour is solid-like [53]. As suggested by Ahn et al. [54] and Bonamy et al. [55], we extract the granular temperature T as the variance of the velocities for a short duration of the flow (0.33 s) by subdividing the drum into elementary square cells of coordinates (x,y) of size set equal to twice the particle diameter. We then define the velocity fluctuation of a particle i as:

$$\delta\varphi_i = \sqrt{\left(\varphi_{i,\ x} - \varphi_{av,x}\right)^2 + \left(\varphi_{i,\ y} - \varphi_{av,y}\right)^2}, \tag{6}$$

where φ_{av} is the mean flow speed value of the cell (x,y) that contains the particle i. From the velocity fluctuation we can compute the granular temperature T_i using:

$$T_i = \frac{1}{2}\delta\varphi_i^2\ . \tag{7}$$

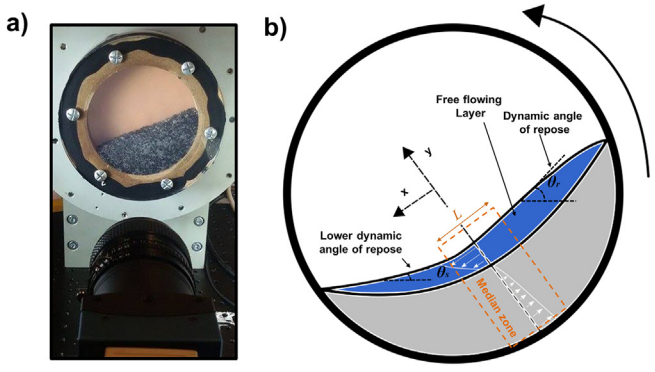

Fig. 4. a) Rotating drum apparatus (back) and camera (front), b) Schematic representation of the particle flow in a rotating drum.

3. Results and discussion

We first examine the effect of particle size and drum rotation speed on the flow characteristics in the dry case using monosized spherical particles. This is followed by results showing the effect of capillary forces on the flow. The obtained data are then used to establish scaling relationships.

3.1. Dry case: effect of particle size and rotation speed on the flow

In a rotating drum, particles are continuously rotated and lifted to the upper part of the drum and the angle of the slope increases until the maximum angle of stability θm (also called avalanching angle) is reached. Once this angle is exceeded, an avalanche occurs and the particles flow, slump or roll down the slope of the flowing layer to a new inferior dynamic angle of repose θr (see Fig. 4 (b)). The maximum angle of stability θm as a function of the Froude number Fr, for the dry case, for particle size $r = 1.25$ mm, is shown in Appendix A. Particles are then coming to rest at the lower part of the bed. There are two important criteria of the avalanche phenomenon for large. First, an avalanche occurs right after the slope of the free surface exceeds a threshold, and a fluid-like flow happens for a period of time equal to the avalanche duration, until the lowest energy state is reached (i.e. particles are at rest). Second, after few rotations of the drum, and for large

Table 2
Properties of the drum and the glass beads.

Properties	Value
Drum, $D \times L$ (mm)	121×22
Glass beads radii r (mm)	0.85, 1.25 and 2
Rotation speed ω (rpm)	5 to 45
Particle density ρ_p, (kg/m^3)	2500
Filling level β	35% (~125 g–0.00035 m^3)
Young's modulus Y (N/m^2)	6.4×10^{10}
Poisson ratio ν	0.2
Volumetric liquid content V_{liq} (ml)	4

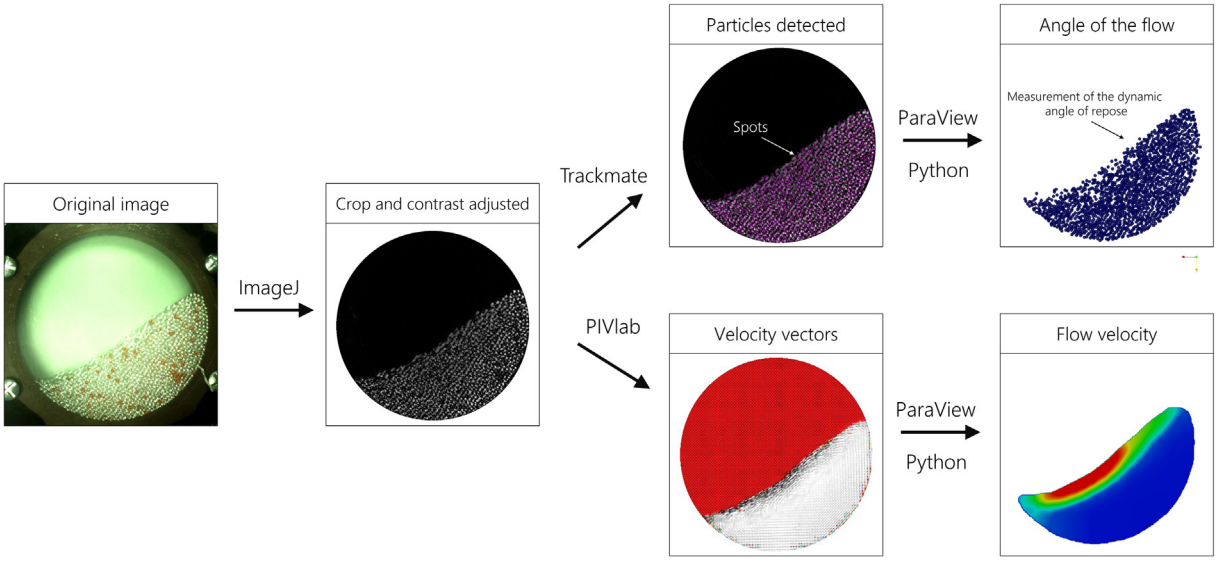

Fig. 5. Post processing steps of the images acquired from the high-speed camera.

enough Froude number ($Fr > 0.05$) a continuous flow regime is reached where $\theta m \approx \theta r$.

As an example, we show in Fig. 6 the dynamic angle of the flow as a function of time for dry particles of radius 1.25 mm and two rotation rates; $\omega = 5$ rpm (i.e. $Fr = 0.04$) and $\omega = 25$ rpm (i.e. $Fr = 0.21$). The drum starts to rotate slowly such that the slope of the interface increases linearly. Then, successive avalanches occur with a stick-slip motion depending on the rotation speed of the drum until a steady continuous flow with small variations is obtained. A complete characterization of the avalanche dynamics of granular media in a rotating drum was carried out by Tegzes et al. [10] and similar behavior of the flow was observed.

Next, we focus on steady continuous flows and we characterize the flow in the drum using the dynamic angle of repose θr and the flow speed profile of the granular assemblies.

Fig. 7 shows the dynamic angle of repose versus the rotation speed for the different particle sizes in the dry case (0.85, 1.25 and 2 mm, case. 1). The dynamic angle of repose increases as the rotation speed increases but the effect of particle size on the dynamic angle of repose is small. Nevertheless, we notice that increasing the particle size slightly decreases the angle of repose at the same rotation speed, possibly due to stronger wall effect (i.e. decreasing $2r/L$).

At low rotation speed (i.e. low Froude number), the error bars of the dynamic angle of repose are large, indicating relatively high variations of the slope of the bed, reminiscent to the slumping intermittent avalanching regime. Around 15 rpm (i.e. $Fr = 0.125$), the error bars of the angle of repose become smaller due the shrinking of the periodicity of the small avalanches occurring in the continuous flow. At around 20 rpm (i.e. $Fr = 0.16$), the S shape starts to form, and the lower dynamic angle of repose decreases with the formation of a curved free surface. At 30 rpm (i.e. $Fr = 0.25$), the flowing layer acquires an even more curved shape, and displays the distinct signatures of the cascading regime. Above 45 rpm (i.e. $Fr = 0.37$), the flow becomes slightly discontinuous marking the transition from the cascading to the cataracting regime. For all particle sizes, when scaling the rotation speed using the

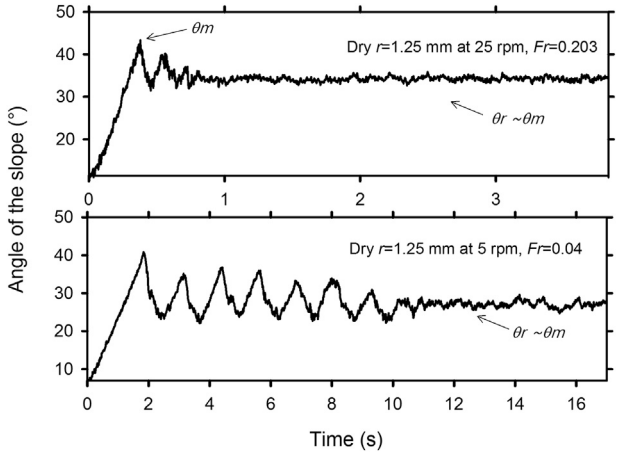

Fig. 6. Transition from avalanching to continuous regime. Glass beads ($r = 1.25$ mm) in a rotating drum.

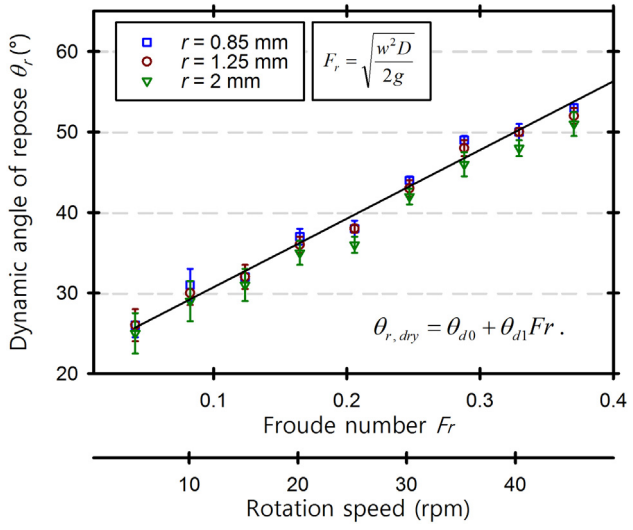

Fig. 7. Dynamic angle of repose θr as a function of the rotation speed and the Froude number Fr, for the dry case. The line is described by Eq. (8).

Froude number *Fr*, the dynamic angle of repose for the dry case collapses into one linear profile (see Fig. 7), with the following equation:

$$\theta_{r,\ dry} = \theta_{d0} + \theta_{d1} Fr \ , \tag{8}$$

with $\theta_{d0} \cong 22^{\circ}$ and $\theta_{d1} \cong 85^{\circ}$.

In Fig. 8 (a), we show the flow velocity components φ_x and φ_y of 1.25 mm particles after 10 s of drum rotation and at 25 rpm ($Fr = 0.203$, in the cascading regime), where the continuous flow is reached. The flow velocity components show a jellyfish cloud where the highest flow speed is observed at the top-right tail, and the lowest is observed at the head of the jellyfish at the bottom-left. Three regions can be distinguished: (1) A flowing region represented by the tail of the jellyfish exhibiting high flow speed comparing to the core of the bed. The maximum flow speed in this region occurs approximately in the centre of the flowing layer. (2) The bottom part of the drum in Fig. 8 (a) represents the static zone where particles are quasi-immobile. Finally (3), a creeping region where the magnitude of the flow speed φ, defined in Section 2.4, increases rapidly with the normal to the flow *y*. We define the boundaries of this region between the interfaces of the static region and the flowing region (i.e. where the velocity magnitude is approximately between 0.1 and 0.25 m/s). In Appendix B, we show also the laboratory frame velocity components v_x and v_y of the flow.

Fig. 8 (b) shows a smoothed field of the flow speed φ averaged over 120 frames (i.e. 0.33 s). In the upper part of the bed, the intensity of φ is the largest, and decreases gradually through the creeping into the static zone. This is because the angular velocity is subtracted from the velocity (see Eq. (5)).

Fig. 8 (c) shows a smoothed field of the granular temperature. Within the core of the bed, the granular temperature is close to zero due to the absence of local velocity fluctuations. This is reminiscent of collective rigid body rotation. However, large fluctuations are observed within the flowing region, with several hot local zones distributed along the upper part of the flowing layer, i.e. near the free surface, which is consistent with Couette flow modelling results of Zhang & Campbell [53]. This indicates high vibrations of the particles due to binary random collisions. In a study of the flow of dry granular material in rotating drums, Chou et al. [56] also found that the granular temperature prevails only in the flowing layer in the rotating drum. This also supports the finding of Bonamy et al. [57], where they demonstrated the presence of clusters in the free flowing layer emitted by the static phase at the bottom of the drum. More qualitative comparison of *T* and φ is presented in next sub-section.

3.2. Wet case: effect of capillary forces

Let us first examine the dynamic angle of repose in the simplest case of non-silanized particles with pure-water as interstitial fluid. This will help us to gain knowledge on the interplay between the effect of the particle size and rotation speed when the particles are wet. The relative velocity in our experiments never exceeds 10 m/s, and since the viscous forces of ethanol and water are very low (0.89 mPa.s for water and 1.074 mPa·s at 25 °C), the capillary number (ratio of the viscous force to the capillary force);

$$Ca = \frac{v_r \mu}{\gamma \cos\theta} \ll 1, \tag{9}$$

with v_r the particle-particle relative velocity and μ the dynamic viscosity of the interstitial liquid, is always below unity. Hence, the capillary forces are more dominant than the viscous forces so the latter can be neglected.

Fig. 9 shows the dynamic angle of repose versus rotation speed in wet systems with pure water as interstitial liquid and for three particle sizes 0.8, 1.25 and 2 mm. Like in the dry case, as the rotation speed increases, the dynamic angle of repose increases. The interparticle liquid cohesion has a significant effect on the bed flow motion. Smaller glass beads have a significantly higher dynamic angle of repose. This is because a decrease of the particle size decreases the capillary force between the particles only a little, but increases the Bond number much more. We observe two regimes; when the rotation speed of the drum is below 35 rpm, the dynamic angle of repose increases linearly with the rotation speed. Above 35 rpm, the capillary force becomes less effective for the case of 2 mm particle size comparing to 0.85 and 1.25 mm, with much reduced increase in the dynamic angles of repose.

We now focus our attention on the effect of the capillary forces on the dynamic angle of repose, flow speed, and granular temperature for the rotation speed of the drum set to 25 rpm ($Fr = 0.203$) and for particles with radius $r = 1.25$ mm. We tune the capillary force by mixing surface treated glass beads (i.e. glass beads of different hydrophobicity) with different ethanol-water mixtures as described in Section 2.1.

The dynamic angle of repose for the wet 1.25 mm particles as a function of the time is shown in Fig. 10 for different capillary force cases. Again, we find that as the capillary force increases, the dynamic angle of repose increases. The angle of the slope of case 7 (wet, non silanized with 0% ethanol) is as big as 49°, consequently, larger than that of dry particles (around 38° in Fig. 7). This is not surprising. As we increase the capillary force at a given rotation rate, the particles experience a greater capillary cohesion and they are dragged more to the upper part of the drum, causing an increase in the slope of the bed. Similar findings were obtained by Nowak et al. [19] and Soria-Hoyo et al. [21] for humid glass beads with constant capillary force. They showed that the angle of the flow decreases with an increase of the particle size for wet particles. Liu et al. [14] found that an increase of the surface tension of the liquid increases the angle of the slope as well as the

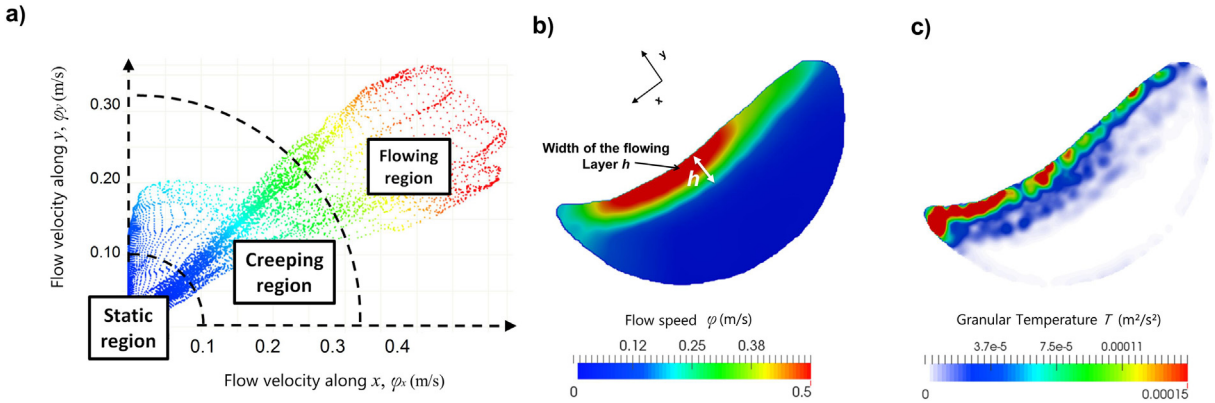

Fig. 8. Snapshots of the a) vertical and horizontal flow velocity components, (b) flow speed φ and (c) granular temperature *T* of the dry bed of 1.25 mm particles at 25 rpm ($Fr = 0.203$).

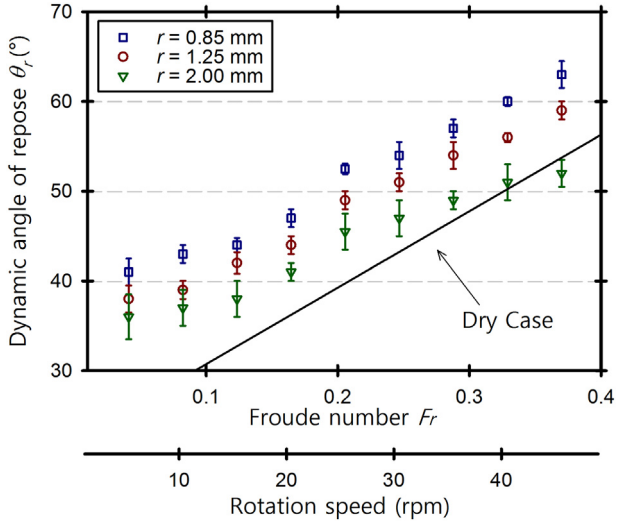

Fig. 9. Dynamic angle of repose as a function of the rotation speed for different particle sizes in the wet case. Dry case line is from Fig. 7.

collision frequency. Furthermore, as expected, silanized glass beads mixed with water show a rather low dynamic angle of repose (case 2) close to that of the dry case. This is because the capillary forces become weaker in the case of silanized surfaces due to the higher glass-liquid contact angle.

For a complete understanding of the flow of wet granular assemblies, we show in Fig. 11 the flow speed φ, granular temperature, and velocity components of the granular flow for particle radius 1.25 mm at 25 rpm and for different capillary forces.

From the flow speed φ field of the drum in the top row of Fig. 11, the flowing layer is easily distinguishable from the static bulk. The slope of the free surface increases with increasing the capillary forces, which confirms the results obtained from the measurement of the dynamic angle of repose. While the flow pattern has a convex shape for dry and low cohesive particles, an almost flat shape is observed for highly cohesive particles, particularly for the 100% (*V*/*V*) water case (case. 7 in Table 1). By visual inspection of φ in Fig. 11, we can see that the flow is confined to a thin layer near the free surface. This layer is composed of the flowing region and the creeping region whose width increases with the capillary forces, and starts to acquire a symmetric profile, suggesting a gradual transition from rapid shear flow to plug flow. At the same time, the surface flow speed seems to decrease with increasing the capillary force. This is despite the fact that the capillary force causes a larger dynamic angle of repose, resulting in a greater kinetic energy from the increase of the down-slope direction of the gravitational acceleration. This decrease of the flow speed can be attributed to two simultaneous effects; one is that the sliding of particles on the free surface is reduced by the cohesion forces exerted by the particles below them; the second effect is that the kinetic energy of the particles is also dissipated by stronger cohesive forces between wet particles. This hints on the coexistence of inertial and capillary forces that governs the flow of wet particles.

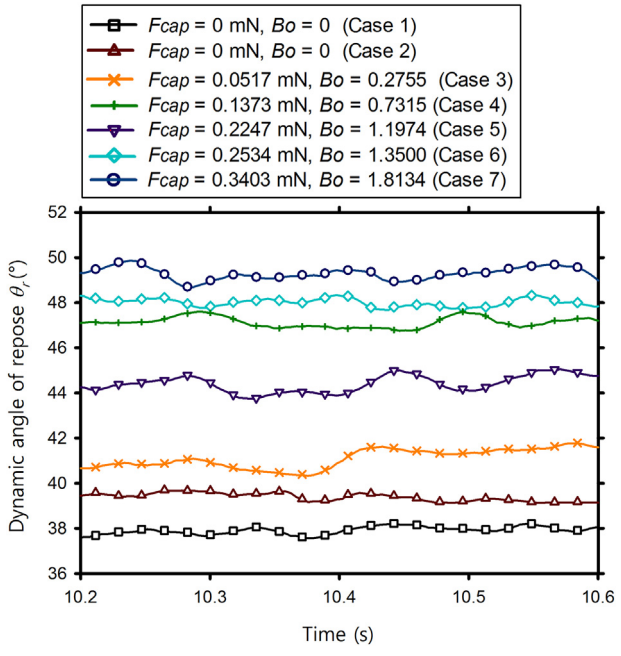

Fig. 10. Smoothed dynamic angle of repose as a function of time in the continuous flow regime for different capillary forces, with particle size $r = 1.25$ mm and drum rotation speed $\omega = 25$ rpm ($Fr = 0.203$).

The values of the granular temperatures in Fig. 11, second row, range from zero near the static zone, up to 0.00015 m^2/s^2 in some spots scattered in the flowing region. The overall average low fluctuations of the flow speed are due to a combination of capillary forces that reduce the collision frequency by cohesion, and a relatively slow flowing regime (i.e. cascading regime). Even though silanized wet glass beads (Case 2) flow almost like dry particles (Fig. 11 (a)), we notice a decrease of the number of hot spots of granular temperature in comparison to the dry case (see Fig. 8 (c)), especially at the left side of the flowing region. Nevertheless, granular flow is still dominated by the inertial forces of the individual particles in the case of silanized beads mixed with water (case 2) because the capillary forces are still weak and the particles can freely roll and move randomly along the free surface. Then, as the capillary force increases, a gradual reduction of the granular temperature in the flowing and creeping regions is observed, indicating less frequent collisions between the particles especially for wet non-silanized cases (Fig. 11 (e) and (f), cases 6 and 7), where the capillary forces are highest. Particles become closely packed and flow as set of clusters rather than individually. This can also be seen in the flow velocity components graph at the bottom of Fig. 11, showing the velocity components of the bed. As the capillary force increases, the jellyfish tail shrinks progressively. This manifests as a less scattered distribution of the *x* and *y* components of the flow velocity in the flowing region, with particles moving in a more orderly fashion on the surface of the bed.

The flow speed φ averaged along the normal to the flow is illuminating this further. To obtain its profile, the flow speed of the particles whose positions are between y and $y + dy$ of the median zone of width L (i.e. particles inside the cubic cell $(y + dy) \times L$) (see Fig. 4 (b)) are averaged and then projected on a line along the y direction:

$$\varphi(y) = \begin{cases} \dfrac{1}{N_y} \displaystyle\sum_{i=1}^{N_y} \varphi_i(y) & \text{if} \quad |x| \le \dfrac{L}{2}, \\ 0 & \text{else}, \end{cases} \tag{10}$$

where N_y is the total number of particles in the cell $(y + dy) \times L$, with L the width of the median zone equals to $4 \times r$ here.

Fig. 12 (a) and (b) shows the spatial distribution along the y axis of the averaged flow speed φ and the granular temperature T, respectively, as obtained using Eq. (7). The granular temperature and the flow speed are plotted from the bottom of the bed, traversing normal to the bed surface (i.e. along y axis) up to the top of the bed. The distance along y is normalized by the width of the bed that goes from the bottom (i.e. 0) of the bed y_0 to its top (i.e. y/y_0).

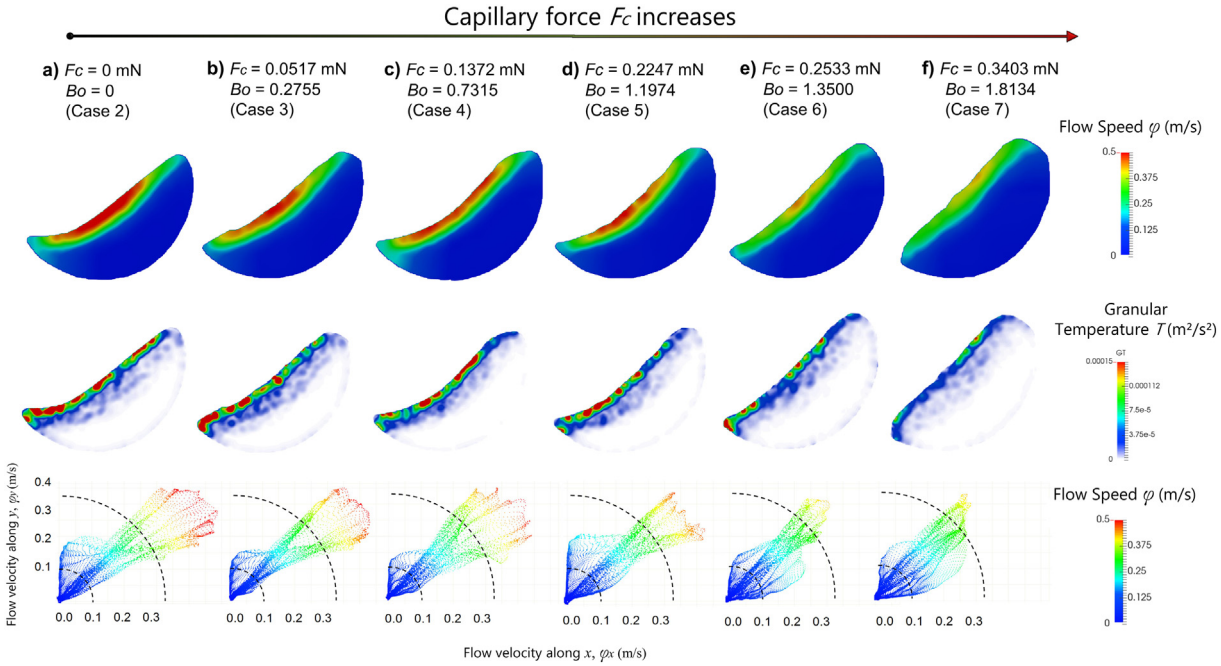

Fig. 11. Snapshots of the flow speed field φ (top), granular temperature T (second row) and the vertical and horizontal flow velocity components of the bed in the rotating drum for different capillary forces. Particles size $r = 1.25$ mm and drum rotation speed $\omega = 25$ rpm.

In Fig. 12 (a), as y/y_0 increases, right after the static region, the flow speed show a rapid rise followed by a steady increase over the creeping region, and finally reaches maxima. This flow speed maxima decrease with the capillary force, with the highest maxima observed for dry glass beads. We attribute this decrease to the formation of cluster network by cohesion. As the clusters increase in size, the bed starts to slip as a bulk of particles interconnected by capillary forces, where each layer of particles is slowed down by the cohesive forces exerted by the layer below. The capillary force between the particles leads to a higher resistance force in the direction opposite to the flow that slow down particle movement along the creeping and the flowing regions. Similar behaviour was obtained by Liao et al. [58] upon increasing the viscosity of an interstitial liquid. By adding glycerol rather than water, these authors found that the flowing layer becomes even thicker and the flow speed decreases even more.

Fig. 12 (b) shows the granular temperature profile along the y axis perpendicular to the flow. Near the wall, because of the solid-like movement of the particles, the granular temperature is almost absent. In the static region, the granular temperature starts to increase slowly, then increases dramatically at the surface and reaches a peak. This indicates a solid-like displacement in the static region, considerable shear with very little granular temperature in the creeping region, and high collision of particles in the flowing regions, confirming the results obtained in Fig. 11. We notice that cases 1 and 2 have the highest granular temperature maxima, and case 7 has the lowest. However, the spots of the granular temperature are not uniform and are dispersed in the creeping and flowing regions (see Fig. 11). This means that the strongly ranging magnitudes of the peaks along the diagonal of the curves in Fig. 12 (b) are not necessarily representative of the effect of the capillary forces on the granular temperature. For this reason, we will examine next the flow characteristics along the surface of the bed.

Similar to Fig. 12, we report in Fig. 13 (a) and (b) the flow speed profile and the granular temperature of the particles, respectively, along the surface. They are both plotted at the surface of the flowing layer, starting from the left, lower side of the drum, crossing the midpoint of the flow to the right, higher side of the drum. The distance along the x axis is normalized by the length of the surface outline (i.e. x/x_0), and the width of the averaged zone L here is also equal to $4 \times r$. In Fig. 13 (a), as expected, the maximum of the flow speed profile decreases with the capillary force. Moreover, the surface profiles exhibit a parabolic shape, skewed to left for the dry case and start to shift to the middle as the capillary force increases. Boateng and Barr [59] observed the same skewness of surface flow in the case of dry materials. They attributed it to the ability of the materials to dissipate energy through collision and gain inertia while flowing down the slope. For the dry case, particles go faster past the mid-chord position, but, once mixed with liquid, they reach their maxima at the midpoint and a symmetric profile is obtained, indicating that the particle flux in the flowing layer midpoint equals the one leaving it. The shifting to the center (symmetrisation) can also be observed in the averaged granular temperature shown in Fig. 13 (b), where the intensity is highest on the left side of the drum for the dry and weakly cohesive cases. This is mainly because the velocity of the particles flowing down from the right side of the bed impacting at the left side is reduced and homogenized by the capillary cohesion. Furthermore, the peaks of the granular temperature decrease with the capillary force. Once again, it can be inferred here that the kinetic energy dissipation in the surface flow due to collision is reduced in favor of energy dissipation due to capillary forces.

Let's examine the effect of the capillary force further by investigating the shear rate in the flowing region. Since the flow speed profile in the midpoint of the creeping region is linear (see Fig. 12 (a)), we can approximate the shear rate on this region using the following formula:

$$\dot{\delta} = \frac{\Delta\varphi}{\Delta y} \tag{11}$$

In Fig. 14, we present the maximal shear rate for particle size 1.25 mm, as a function of capillary force and rotation speed. We vary the

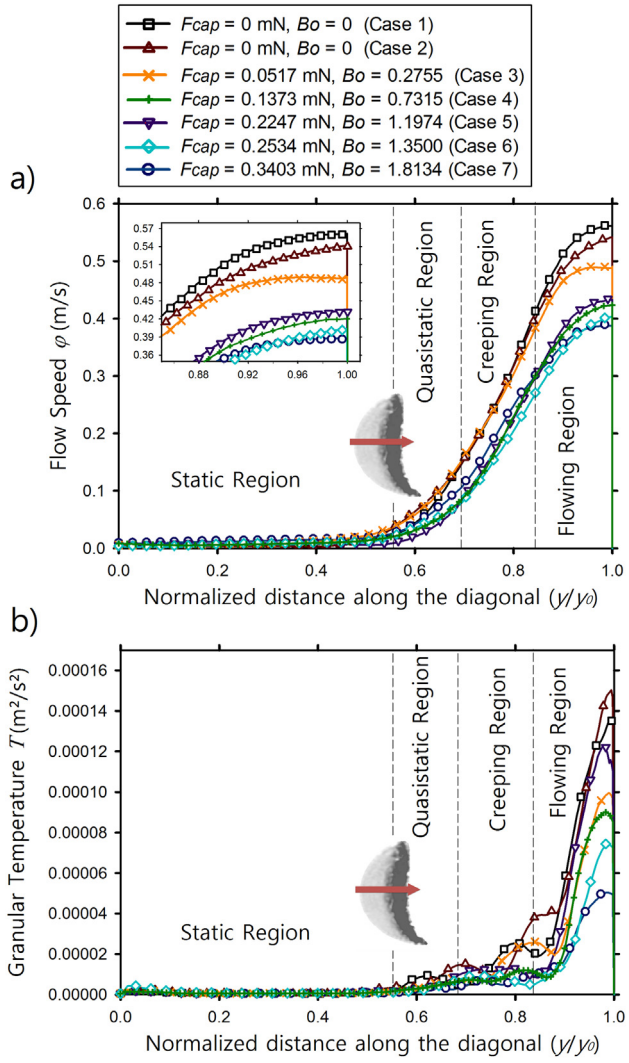

Fig. 12. a) Averaged flow speed φ profile along the diagonal (y/y_0) normal to the free surface. b) Averaged granular temperature profile along the diagonal (y/y_0) normal to the free surface, with particle size $r = 1.25$ mm and drum rotation speed $\omega = 25$ rpm.

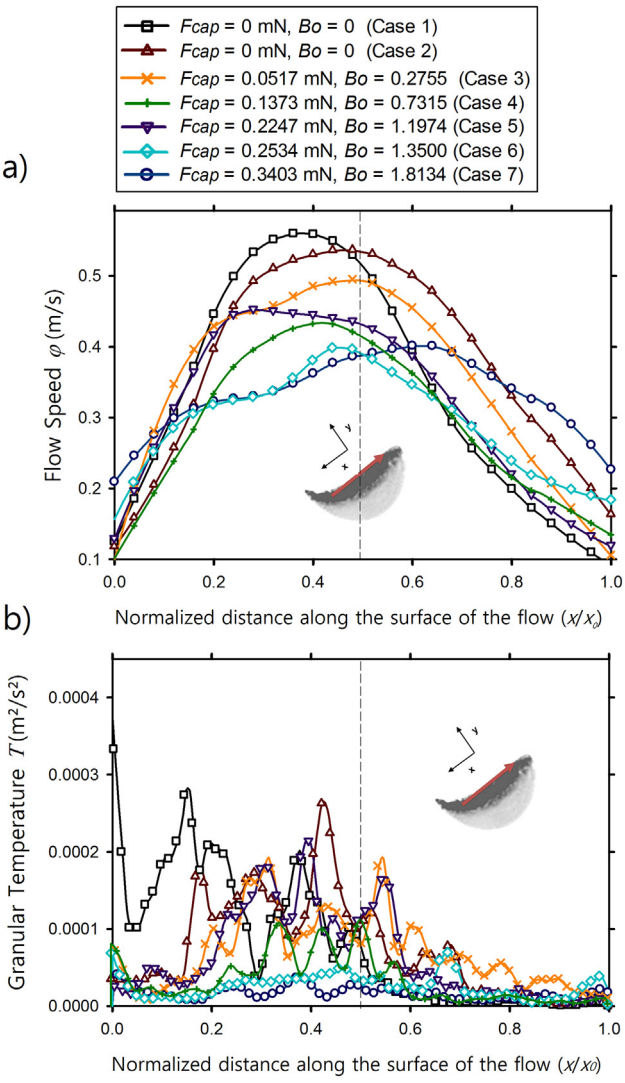

Fig. 13. a) Averaged flow speed φ profile along the surface (x/x_0), b) Averaged granular temperature profile along the surface of the flow (x/x_0). Particles size $r = 1.25$ mm and drum rotation speed $\omega = 25$ rpm.

rotation speed for wet particles with 100% (V/V) water (case 7) and we present the data with cross red symbols in Fig. 14. We also vary the capillary force for drum rotation speed of 25 rpm and we present the data as square symbols in Fig. 14. The values of the shear rate were calculated from the slope of the linear part of the velocity profiles using Eq. (11). The shear rate increases linearly with an increase of the rotation speed. This is a direct result of the increase of the flow speed. This latter increases the sliding of the flowing layer, which in turn increases the shear rate in the creeping region. However, the shear rate slightly decreases with the increase of the capillary force, due to higher kinetic energy dissipation and less particle collisions due to stronger capillary attraction. Overall, the effect the capillary force on the shear rate is low comparing to that of the rotation speed of the drum.

3.3. Scaling of wet granular flow

The concept of similarity based on dimensional analysis states that two processes might be considered similar if all involved length scales are proportional, and all dimensionless numbers needed to describe them have the same value [18,60].

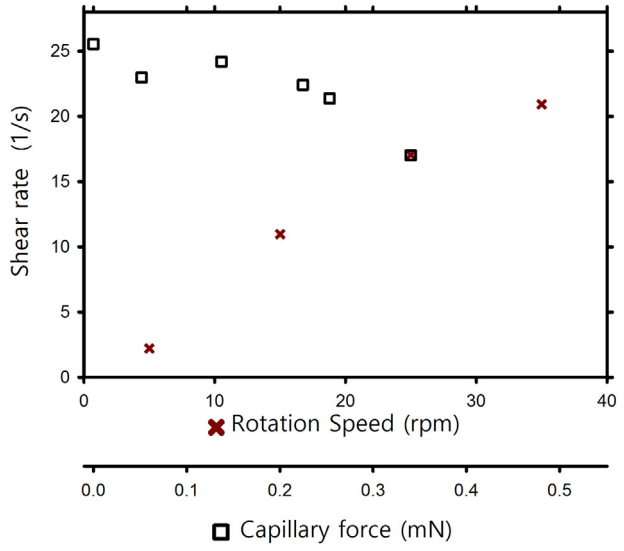

Fig. 14. Shear rate in the creeping region as a function of the capillary force at 25 rpm, and as a function of rotation speed at 100% (V/V) water, case 7.

Five dimensionless groups are presented in Eq. (12) including the Froude number *Fr* (ratio of inertial force to gravity force), granular Weber number *We* (i.e. ratio of inertial forces to capillary forces), bed saturation *s*, capillary number *Ca*, and drum fill ratio β.

$$Fr = \sqrt{\frac{\omega^2 D}{2g}},\quad We = \frac{\rho_p r v^2}{\gamma \cos\theta},\quad s = \frac{V_{liq}}{V_{bed}\xi}\ ,\quad Ca = \frac{v_r \mu}{\gamma \cos\theta}\ , \tag{12}$$

where N_p is the total number of particles. Notice that the Weber and Capillary numbers in eq. (12) take into consideration the effect of the particle-liquid contact angle θ.

For scaling, we have kept liquid-particle volume ratio, and drum fill percentage constant among all experiments. We scale the dynamic angle of repose of wet particles using the Weber number. As emphasized previously, the effect of capillary forces on the flow speed is low comparing to the effect of the rotation speed of the drum. Hence, we will define the average velocity in the Weber number equation equal to the rotation speed of the drum times its radius (i.e. $w \times D/2$), and we focus on the effect of the Weber number on the flow where the capillary forces are dominant (i.e. capillary number $Ca \ll 1$). In Fig. 15, we show the evolution of the dynamic angle of repose as a function of the inverse of the granular Weber number. We vary the Weber number by varying the particle size for different capillary forces (cases 3 to 7 in Table 1, for 0.85, 1.25 and 2 mm particles) for a fixed rotation speed $\omega = 25$ rpm. The dynamic angle of repose increases with the inverse of the Weber number and shows an exponential rise:

$$\theta_{r,\,fit} = \theta_{r1} - (\theta_{r1} - \theta_{r0}) e^{-\left(\frac{We_\theta}{We}\right)^b}, \tag{13}$$

with $\theta_{r1} \cong 56^\circ$, $We_\theta = 45.24$, $b = 0.713$ and $\theta_{r0} = \theta_{r,\ dry} \cong 37^\circ$ is the angle at which the inverse of Weber number is equal to zero (the dry case at 25 rpm). The collapse of the data indicates that points with close Weber number have similar dynamic angle of repose. This allows to maintain dynamic similarity after scaling the particle size. We will test this hypothesis by changing the particle size while keeping the Weber number constant by increasing the capillary force accordingly.

The points inside the red dashed circle in Fig. 15 have the same *We* for different particle sizes: 2, 1.25 and 0.85 mm with three different cases: case 7, case 4 and case 3, respectively (case 7: Water with non-silanized glass beads, case 4: mixture of 10% ethanol-90% water (*V*/*V*) with silanized glass beads, case 3: mixture of 20% ethanol-80% water

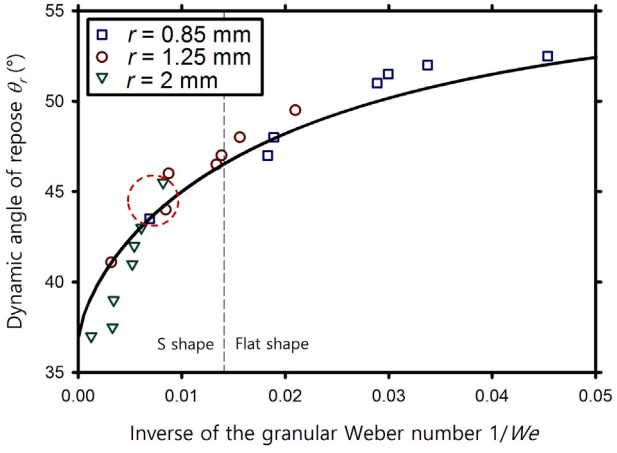

Fig. 15. Dynamic angle of repose θ_r with its respective fitted curve, plotted against the granular Weber number. Drum rotation speed: 25 rpm.

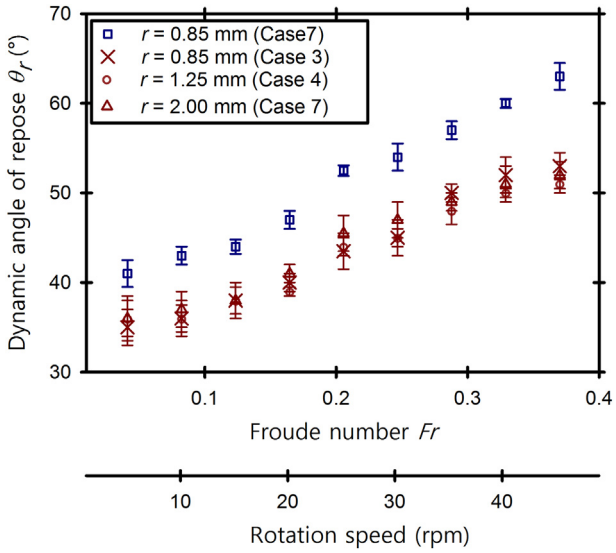

Fig. 16. Dynamic angle of repose as a function of the rotation speed for different particle sizes in the wet case, for similar $We \approx 120$ (red symbols), and one case (blue squares) with highly different $We \approx 22$.

(*V*/*V*) with silanized glass beads, see Table 1). We compare those three points and check whether they have the same dynamic angle of repose for different rotation speeds of the drum.

Fig. 16 presents the dynamic angle of repose of wet samples for different rotation speeds. While the red symbols represent the three points that we chose (inside the red circle in Fig. 15) of different particle sizes with almost the same Weber number, solid blue symbols represent non-silanized particles of size 0.85 mm mixed with 100% (*V*/*V*) water (case 7) and lower Weber number as a reference to indicate the range of θ_r.

The dynamic angle of repose of the chosen points (i.e. particle sizes 2, 1.25 and 0.85 mm) fall onto a single curve, indicating that 2 mm particles can be rescaled to 0.85 mm or 1.25 mm sizes if the Weber number is kept constant. This means that, experimentally, the scaling approach works in the considered flow regimes (rolling and cascading).

Let us explore further this scaling and look closer at the flow speed φ of these three points (inside the red circle in Fig. 15) with the same Weber number. Similarly to subsection 3.2, we plot in Fig. 17 (a) and (b), the flow speed profiles at the midpoint of the flow along the diagonal and on the surface of the flow, respectively. The blue square symbols, as before, represent wet particles with 100% (*V*/*V*) water (case 7, $r = 0.85$ mm) with different *We*. In the flowing region, the profiles of the red symbols curves are very close to each other but far away from the blue curve, especially in the case of the diagonal φ profile in Fig. 17 (a). The flow speed at the surface is the same for the three particle sizes (in red). In Fig. 17 (b), small lateral variations are observed for flow speed along the surface of the red curves, especially in the case of 2 mm particle size, but still, here also, they show similar profiles relative to the blue case that display much smaller φ.

Since the dynamic angle of repose of dry particles can be scaled with the Froude number as we already showed in Fig. 7, we will develop a scaling equation that takes into consideration the rotation speed. We will focus on the ratio of the angles of repose of the wet to the dry case:

$$\Delta\theta = \frac{\theta_{r,\ wet}}{\theta_{r,\ dry}}\ . \tag{14}$$

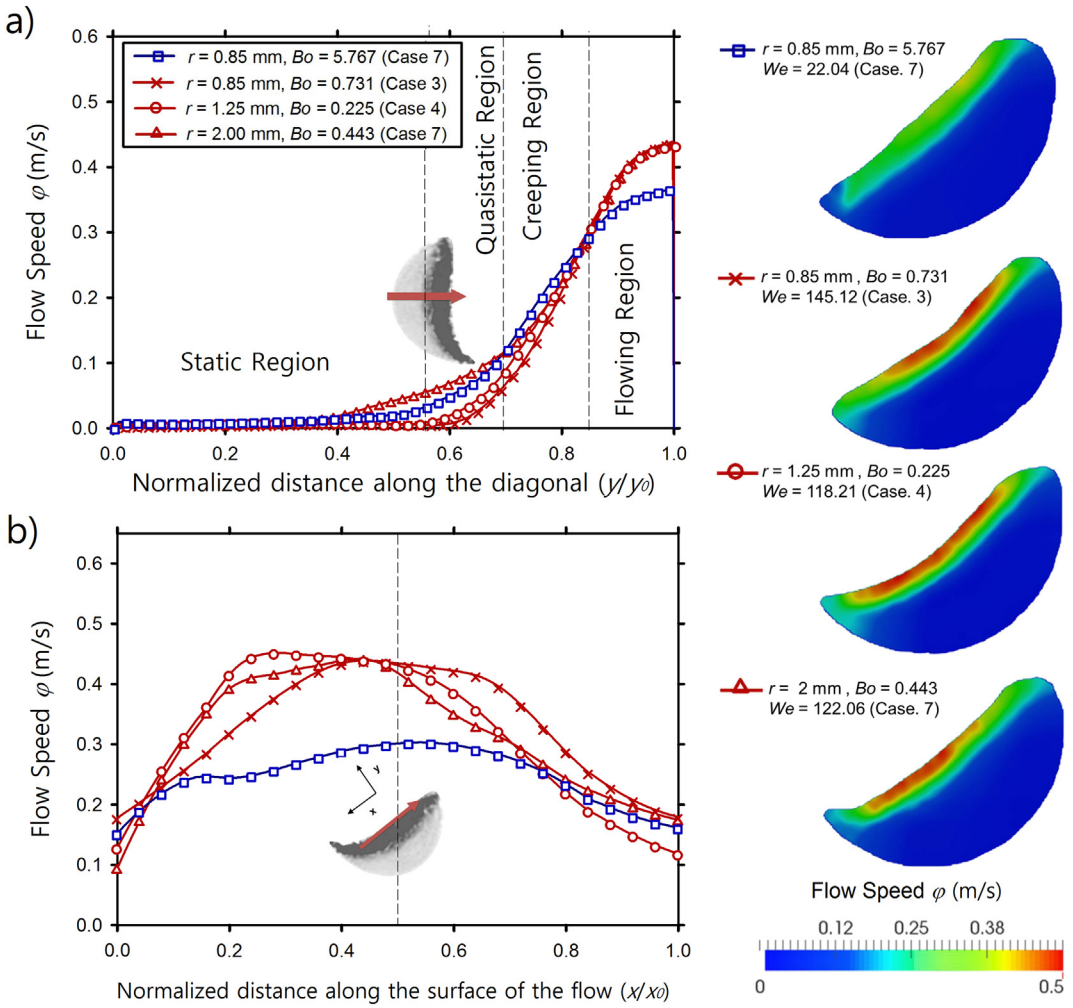

Fig. 17. a) Average flow speed φ profile along the diagonal (y/y_0) normal to the free surface, b) Average flow speed φ profile along the surface of the flow (x/x_0). Drum rotation speed $\omega =$ 25 rpm.

In Fig. 18, we plot $\Delta\theta$ as a function of the inverse of the Weber number for different rotation speeds and different particle sizes, where $\theta_{r,\ wet}$ and $\theta_{r,\ dry}$ are the dynamic angles of repose in the wet and dry cases, respectively. The ratio increases linearly with the inverse of the Weber number and all the points seem to collapse into a single master curve with a standard error of 0.0303. Fig. 18 can be used to predict and control the flow of the particles from the surface properties of glass beads and the adequate ethanol-water fraction.

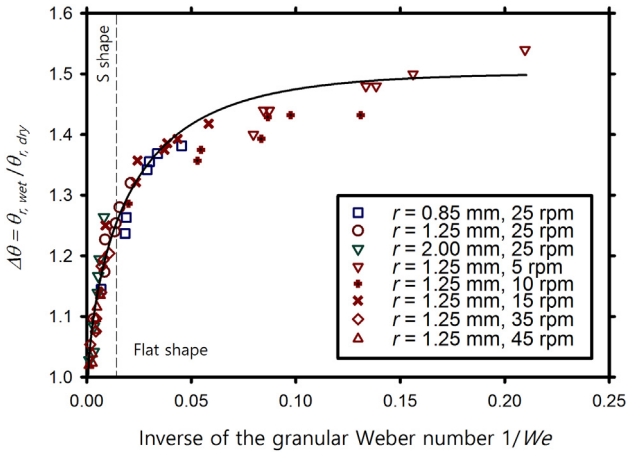

Fig. 18. Ratio of the wet over the dry dynamic angle of repose, $\Delta\theta$ plotted against the granular Weber number with its fitted curve from Eq. (14).

The curve fit obtained in Fig. 18 is described by the following equation:

$$\Delta\theta_{fit} = \frac{\theta_{r,\ fit}}{\theta_{dry}} \quad , \tag{15}$$

with $\theta_{r,\ fit}$ the fitted dynamic angle of repose obtained using eq. (13) and θ_{dry} can be calculated using eq. (8).

4. Conclusion

Experiments on the continuous flow in a rotating drum of dry and wet granular material were reported in this paper. The effect of capillary forces and the particle size on the flow characteristics was investigated for different rotation speeds. We have extracted granular temperature and flow speed profiles by means of statistical analysis and PIV. We established a scaling relationship using the Froude and the Weber number and we showed that the

dynamic angle of repose and the shape of the free surface can be varied and controlled to be similar by combining the rotation rate of the drum and the capillary forces into an empirical scaling relation.

We demonstrated that chemical salinization of the glass beads allows to continuously alter the capillary forces between the particles, allowing to investigate the flow of granular assembly over a wide range of capillary forces. We showed that the presence of liquid increases the depth of the flowing layer and reduces the flow speed of the particles. Granular temperature snapshots showed that capillary forces reduce particle collisions due to of kinetic energy dissipation by cohesion forces. When the cohesion between particles increases, particles become more closely packed and act as clusters rather than individually. Capillary forces lead to a greater resistance force exerted by the core of the bed on the flowing region, resulting in a slower flow speed and thus, decrease the shear rate in the flowing region. Finally, we proposed a scaling methodology that ensures similarity of the dynamic angle of repose by keeping the Weber number and the Froude number constant after scaling the particle radius. We were able to obtain similar bed flow for different particle sizes, and confirmed that the proposed scaling approach works for the rolling and cascading regimes.

The results reported here open several prospects. For instance, it would be interesting to include the effect of the liquid viscosity on the rather dynamic bed flow and to look deeper into the microstructure of the wet granular flow using Discrete Element Method (DEM), which will be the focus of future work. It would be of great interest also to consider how well the scaling methodology works in other flowing regimes such as the cataracting regime. Moreover, this paper provided some important clarifications regarding the capillary force effects on the local internal flow dynamics of granular assemblies that should be applied to and checked against other granular flows simulations (e.g. silo, inclined plane, chute flow, etc.).

List of symbols

Ca	Capillary number	[−]
D	Drum diameter	[m]
d	Distance between 2 particles surfaces	[m]
F_c	Capillary force	[N]
Fr	Froude number	[−]
g	Gravitational acceleration	[m/s^2]
k	Mass fraction of liquid	[−]
L	Width of the drum	[m]
N_p	Total number of particles in the drum	[−]
r	Particle radius	[m]
T	Granular temperature	[m^2/s^2]
V_{bed}	Volume of the bed	[m^3]
V_{liq}	Volume of liquid added	[m^3]
v	Particle velocity	[m/s]
v_r	Relative velocity of the particles	[m/s]
v_ω	Angular velocity of the particle	[1/s]
We	Weber number	[−]
s	Bulk saturation	[−]
Y	Young's modulus Y	[N/m^2]
ν	Poisson ratio ν	[−]
θ	Contact angle	[°]
θ_r	Dynamic angle of repose	[°]
θ_m	Maximum angle of stability	[°]
θ_s	Lower dynamic angle of repose	[°]
γ	Surface tension	[N/m]
$\boldsymbol{\omega}$	Rotation speed	[s^{-1}]
ρ_p	Particle density	[kg/m^3]
β	Filling level of the drum	[−]
μ	Dynamic viscosity of the interstitial liquid	[Pa.s]
φ	Flow speed	[m/s]
$\dot{\delta}$	Shear rate	[1/s]

Acknowledgements

We thank Andries van Swaaij (Dries), Harmen Polman, Marco Ramaioli, Luca Orefice and Bert Scheper for their help. We also thank Prof. Johannes Khinast for his feedbacks. Financial support through the "T-MAPPP" project of the European-Union-Funded Marie Curie Initial Training Network FP7 (ITN607453) is acknowledged.

Appendix A

Fig. A.1 shows the maximum angle of stability θm as a function of the Froude number Fr, which increases weakly with the Froude number and exhibits high variability especially at low rotation speeds. When the Froude number increases, the rotation time becomes too short compared to the avalanche duration, which explains the decrease of the variability with the Froude number.

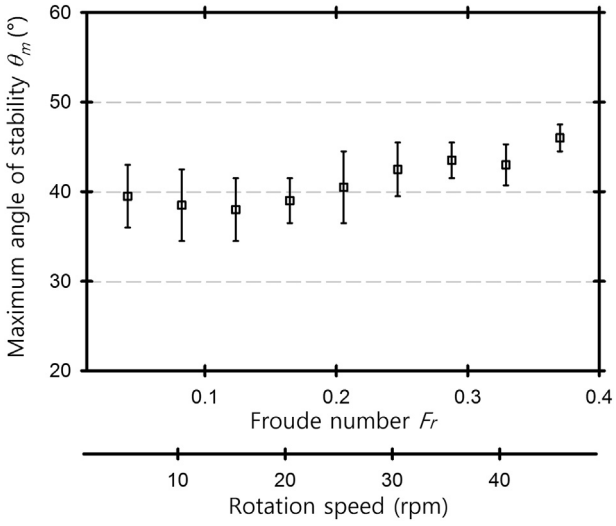

Fig. A.1. Maximum angle of stability θm as a function of the rotation speed and the Froude number Fr, for the dry case, for particle size $r = 1.25$ mm.

Appendix B

Fig. B.1 shows the velocity v components of the bed in a rotating drum for different capillary forces. The three zones; flowing, creeping and static are easily distinguishable in Fig. B.1 (a). The wall driven (i.e. solid body rotating with the drum) velocity is observed at the thick head of the jellyfish at the bottom-left and the flowing zone is spread on the tail of the jellyfish shape. The flow velocity profiles of the wet case and the dry case of the jellyfish can be found in our previous work [18] and in the work of Weinhart et al. [61]. As the capillary force increases the tail of the jellyfish shrinks indicating tighter distributions of the velocity components, confirming the results shown in Fig. 11. The median angle made by the cloud of the velocity components in the creeping region is approximately equal to $(\theta r + \theta s)/2$. The particles as well as the velocity components distribution are less scattered and denser in this region comparing to the other regions (see Fig. B.1 (a)). As explained by Komatsu [8], the particles in the static region inhibit the displacement of those outside this region.

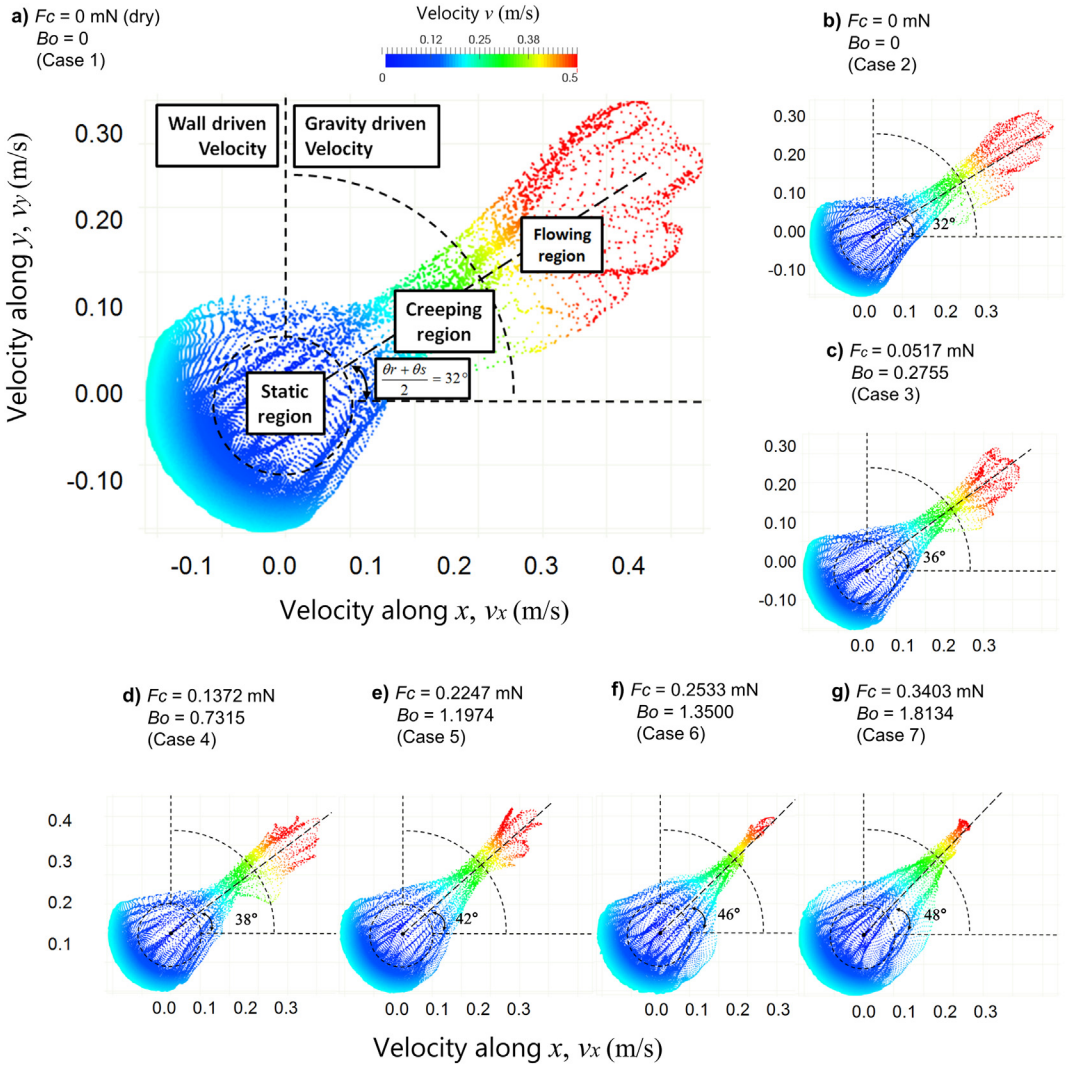

Fig. B.1. Snapshots of the velocity's vertical and horizontal components in the rotating drum for different capillary forces. Particles size $r = 1.25$ mm and drum rotation speed $\omega = 25$ rpm.

Appendix C. Supplementary data

Supplementary data to this article can be found online at https://doi.org/10.1016/j.powtec.2018.02.045.

References

[1] H. Henein, J.K. Brimacombe, A.P. Watkinson, Experimental study of transverse bed motion in rotary kilns, Metall. Trans. B 14 (1983) 191–205.
[2] J. Rajchenbach, Flow in powders: from discrete avalanches to continuous regime, Phys. Rev. Lett. 65 (1990) 2221.
[3] N. Taberlet, P. Richard, E.J. Hinch, The S-shape of a granular pile in a rotating drum, Phys. Rev. E 73 (2006), 050301.
[4] A.V. Orpe, D.V. Khakhar, Scaling relations for granular flow in quasi two-dimensional rotating cylinders, Phys. Rev. E 64 (2001), 031302.
[5] T. Elperin, A. Vikhansky, Granular flow in a rotating cylindrical drum, Europhys. Lett. 42 (1998) 619–623.
[6] L.T. Sheng, W.C. Chang, S.S. Hsiau, Influence of particle surface roughness on creeping granular motion, Phys. Rev. E 94 (2016), 012903.
[7] M. Nakagawa, S. Altobelli, A. Caprihan, E. Fukushima, E. Jeong, Non-invasive measurements of granular flows by magnetic resonance imaging, Exp. Fluids 16 (1993) 54–60.
[8] T. Komatsu, S. Inagaki, N. Nakagawa, S. Nasuno, Creep motion in a granular pile exhibiting steady surface flow, Phys. Rev. Lett. 86 (2001), 101103.
[9] N. Jain, J.M. Ottino, R.M. Lueptow, An experimental study of the flowing granular layer in a rotating tumbler, Phys. Fluids 14 (2002) 572–582.
[10] P. Tegzes, T. Vicsek, P. Schiffer, Development of correlations in the dynamics of wet granular avalanches, Phys. Rev. E 67 (2003), 051303.
[11] H. Schubert, Capillary forces — modeling and application in particulate technology, Powder Technol. 37 (1984) 105–116.
[12] R. Brewster, G.S. Grest, A.J. Levine, Effects of cohesion on the surface angle and velocity profiles of granular material in a rotating drum, Phys. Rev. E 79 (2009) 1–7 (011305).
[13] S.H. Chou, C.C. Liao, S.S. Hsiau, An experimental study on the effect of liquid content and viscosity on particle segregation in a rotating drum, Powder Technol. 201 (2010) 266–272.
[14] P.Y. Liu, R.Y. Yanga, A.B. Yu, Dynamics of wet particles in rotating drums: Effect of liquid surface tension, Phys. Fluids 23 (2011) 1–9 (013304).
[15] A. Samadani, A. Kudrolli, Segregation transitions in wet granular matter, Phys. Rev. Lett. 85 (2000) 5102–5105.
[16] S. Roy, A. Singh, S. Luding, T. Weinhart, Micro–macro transition and simplified contact models for wet granular materials, Comp. Part. Mech. 3 (2016) 449–462.
[17] R. Mani, D. Kadau, H.J. Herrmann, Liquid migration in sheared unsaturated granular media, Granul. Matter 15 (2013) 447–454.
[18] A. Jarray, V. Magnanimo, M. Ramaioli, S. Luding, Scaling of wet granular flows in a rotating drum, EPJ Web of Conferences, Powders and Grains, 140, 2017, pp. 1–4 (03078).
[19] S. Nowak, A. Samadani, A. Kudrolli, Maximum angle of stability of a wet granular pile, Nat. Phys. 1 (2005) 50–52.
[20] Q. Xu, A.V. Orpe, A. Kudrolli, Lubrication effects on the flow of wet granular materials, Phys. Rev. E 76 (2007), 031302.
[21] C. Soria-Hoyo, J.M. Valverde, A. Castellanos, Avalanches in moistened beds of glass beads, Powder Technol. 196 (2009) 257–262.
[22] D. Hornbaker, R. Albert, I. Albert, A.L. Barabasi, P. Schiffer, What keeps sandcastles standing? Nature 387 (1997) 765.
[23] M.M. Kohonena, D. Geromichalosb, M. Scheelb, C. Schierb, S. Herminghaus, On capillary bridges in wet granular materials, Physica A 339 1–2 (2004) 7–15.
[24] J.E. Fiscina, G. Lumay, F. Ludewig, N. Vandewalle, Compaction dynamics of wet granular assemblies, Phys. Rev. Lett. 105 (2010), 048001.
[25] R. Schwarze, A. Gladkyy, F. Uhlig, S. Luding, Rheology of weakly wetted granular materials — a comparison of experimental and numerical data, Granul. Matter 15 (4) (2013) 455–465.

[26] Z. Fournier, D. Geromichalos, S. Herminghaus, et al., Mechanical properties of wet granular materials, J. Phys. Condens. Matter 17 (2005) S477–S502.
[27] T. Gillespie, W.J. Settineri, The effect of capillary liquid on the force of adhesion between spherical solid particles, J. Colloid Interface Sci. 24 (1967) 199–202.
[28] R.A. Fisher, On the capillary forces in an ideal soil, J. Agric. Sci. 16 (1926) 492–505.
[29] T.C. Halsey, A.J. Levine, How sandcastles fall, Phys. Rev. Lett. 80 (1998) 3141.
[30] J.N. Israelachvili, Intermolecular and Surface Forces (Academic Press), University of California, 2010.
[31] Y.I. Rabinovich, M.S. Esayanur, B.M. Moudgil, Capillary forces between two spheres with a fixed volume liquid bridge: theory and experiment, Langmuir 21 (2005) 10992–10997.
[32] P.S. Raux, H. Cockenpot, M. Ramaioli, D. Quéré, C. Clanet, Wicking in a powder, Langmuir 29 (11) (2013) 3636–3644.
[33] A.F. Stalder, T. Melchior, M. Müller, D. Sage, T. Blu, Low-bond axisymmetric drop shape analysis for surface tension and contact angle measurements of sessile drops, Colloids Surf. A Physicochem. Eng. Asp. 364 (2010) 72–81.
[34] G. Vazquez, E. Alvarez, J.M. Navaza, Surface tension of alcohol water + water from 20 to 50 °C, J. Chem. Eng. Data 40 (3) (1995) 611–614.
[35] M.H. Klein Schaarsberg, I.R. Peters, M. Stern, K. Dodge, et al., From splashing to bouncing: the influence of viscosity on the impact of suspension droplets on a solid surface, Phys. Rev. E 93 (2016), 062609.
[36] Q. Xu, I. Peters, S. Wilken, E. Brown, H. Jaeger, Fast imaging technique to study drop impact dynamics of non-Newtonian fluids, J. Vis. Exp. (85) (2014), 51249.
[37] M. Tagawa, K.J. Gotoh, Y. Nakagawa, Penetration of water/ethanol mixtures into silanized silica fibrous assemblies, J. Adhes. Sci. Technol. 12 (1998) 1341–1353.
[38] C.R.K. Windows-Yule, B.J. Scheper, A.J. van der Horn, N. Hainsworth, J. Saunders, D.J. Parker, A.R. Thornton, Understanding and exploiting competing segregation mechanisms in horizontally rotated granular media, New J. Phys. 18 (2016) 1–17 (023013).
[39] N. Jain, J.M. Ottino, R.M. Lueptow, Regimes of segregation and mixing in combined size and density granular systems: an experimental study, Granul. Matter 7 (2005) 69–81.
[40] T. Arndt, A. Brucks, J.M. Ottino, R.M. Lueptow, Creeping granular motion under variable gravity levels, Phys. Rev. E 74 (2006) 1–7 (031307).
[41] G. Juarez, P. Chen, R.M. Lueptow, Transition to centrifuging granular flow in rotating tumblers: a modified Froude number, New J. Phys. 13 (2011), 053055.
[42] J. Litster, B. Ennis, The Science and Engineering of Granulation Processes, 15, Springer, 2004 250 (Netherlands).
[43] A.D. Salman, M.J. Hounslow, J.P.K. Seville, Granulation. Handbook of Powder Technology, 11, Elsevier, 2007 1390.
[44] J.Y. Tinevez, N. Perry, et al., TrackMate: an open and extensible platform for single-particle tracking, Methods 115 (2017) 80–90.
[45] D.G. Lowe, Distinctive image features from scale-invariant keypoints, Int. J. Comput. Vis. 60 (2004) 91–110.
[46] A. Henderson, A ParaView Guide: Parallel Visualization Application, Kitware Inc., 2007
[47] A.L. Chaua, X. Lia, W. Yu, Convex and concave hulls for classification with support vector machine, Neurocomputing 122 (2013) 198–209.
[48] W. Thielicke, E.J. Stamhuis, PIVlab – towards user-friendly, affordable and accurate digital particle image velocimetry in MATLAB, J. Open Res. Softw. 2 (1) (2014) 1–10 (e30).
[49] H. Abram Clark, L. Kondic, R.P. Behringer, Steady flow dynamics during granular impact, Phys. Rev. E 93 (2016), 050901.
[50] A. Seguin, Y. Bertho, F. Martinez, J. Crassous, P. Gondret, Experimental velocity fields and forces for a cylinder penetrating into a granular medium, Phys. Rev. E 87 (2013), 012201.
[51] W. Schroeder, K. Martin, B. Lorensen, The Visualization Toolkit: An Object-Oriented Approach to 3D Graphics, 4th edition Kitware, United states, 2006.
[52] D.J. Price, Smoothed particle hydrodynamics and magnetohydrodynamics, J. Comput. Phys. 231 (2012) 759–794.
[53] Y. Zhang, C.S. Campbell, The interface between fluid-like and solid-like behaviour intwo-dimensional granular flows, J. Fluid Mech. 237 (1992) 541–568.
[54] H. Ahn, C.E. Brennen, R.H. Sabersky, Measurements of velocity, velocity fluctuation, density, and stresses in chute flows of granular materials, Trans. ASME J. Appl. Mech. 58 (1991) 792–803.
[55] D. Bonamy, P.H. Chavanis, P.P. Cortet, F. Daviaud, B. Dubrulle, M. Renouf, Euler-like modelling of dense granular flows: application to a rotating drum, Euro. Phys. J. B 68 (4) (2009) 619–627.
[56] H.T. Chou, C.F. Lee, Cross-sectional and axial flow characteristics of dry granular material in rotating drums, Granul. Matter 11 (2009) 13–32.
[57] D. Bonamy, F. Daviaud, L. Laurent, M. Bonetti, J.P. Bouchaud, Multiscale clustering in granular surface flows, Phys. Rev. Lett. 89 (2002), 034301.
[58] C.C. Liao, S.S. Hsiau, Kiwing To, Granular dynamics of a slurry in a rotating drum, Phys. Rev. E 82 (2010) (010302R).
[59] A.A. Boateng, P.V. Barr, Granular flow behaviour in the transverse plane of a partially filled rotating cylinder, J. Fluid Mech. 330 (1997) 233–249.
[60] F.M. Henderson, Open Channel Flow, Macmillan Publishing Co., Inc., New York, 1966 522.
[61] T. Weinhart, D.R. Tunuguntla, A. Jarray, S. Luding, ... A.R. Thornton, MercuryDPM: Fast, flexible particle simulations in complex geometries part II: Applications, 5th International Conference on Particle-Based Methods - Fundamentals and Applications, PARTICLES, 2017, 2017, pp. 123–134.